Magnetostriction-driven ground-state stabilization in 2H perovskites

D. G. Porter,[1,*] M. S. Senn,[1,2] D. D. Khalyavin,[3] A. Cortese,[4] N. Waterfield-Price,[1,5] P. G. Radaelli,[5] P. Manuel,[3] H.-C. zur-Loye,[4] C. Mazzoli,[6,7] and A. Bombardi[1,5]

[1]*Diamond Light Source Ltd., Harwell Science and Innovation Campus, Didcot, Oxfordshire, OX11 0DE, United Kingdom*
[2]*Inorganic Chemistry Laboratory, University of Oxford South Parks Road, Oxford OX1, 3QR, United Kingdom*
[3]*ISIS Facility, Rutherford Appleton Laboratory-STFC, OX11 0QX, Chilton, Didcot, United Kingdom*
[4]*Department of Chemistry & Biochemistry, University of South Carolina, Columbia, South Carolina 29208, USA*
[5]*Department of Physics, University of Oxford, Parks Road, Oxford OX1 3PU, United Kingdom*
[6]*VI Dip.to di Fisica, unità CNISM, Politecnico di Milano, Piazza Leonardo Da Vinci 32, 20133 Milano, Italy*
[7]*National Synchrotron Light Source II, Brookhaven National Laboratory, Upton, New York 11973, USA*

(Received 14 July 2016; revised manuscript received 7 September 2016; published 4 October 2016)

The magnetic ground state of Sr_3ARuO_6, with A = (Li,Na), is studied using neutron diffraction, resonant x-ray scattering, and laboratory characterization measurements of high-quality crystals. Combining these results allows us to observe the onset of long-range magnetic order and distinguish the symmetrically allowed magnetic models, identifying in-plane antiferromagnetic moments and a small ferromagnetic component along the c axis. While the existence of magnetic domains masks the particular in-plane direction of the moments, it has been possible to elucidate the ground state using symmetry considerations. We find that due to the lack of local anisotropy, antisymmetric exchange interactions control the magnetic order, first through structural distortions that couple to in-plane antiferromagnetic moments and second through a high-order magnetoelastic coupling that lifts the degeneracy of the in-plane moments. The symmetry considerations used to rationalize the magnetic ground state are very general and will apply to many systems in this family, such as Ca_3ARuO_6, with A = (Li,Na), and Ca_3LiOsO_6 whose magnetic ground states are still not completely understood.

DOI: 10.1103/PhysRevB.94.134404

I. INTRODUCTION

The variant of the hexagonal (2H) perovskite structure of general formula $A_{3n+3m}A'_nB_{3m+n}O_{9m+6n}$ has recently been the subject of extensive investigations. The structure, whose prototype is Sr_4PtO_6 ($n = 1$, $m = 0$), consists of infinite chains of trigonal prisms and slightly distorted octahedra. In this peculiar arrangement, magnetic ions sit within the octahedra, the trigonal prism or at both sites, offering a fertile ground for the investigation of a range of phenomena. For instance, diluting the trigonal prisms along the c axis with varying the m/n ratio leads to valence disproportionations [1], whereas the arrangement in chains can be readily connected with dimensionality effects [2]. In this paper we will focus on systems with $m = 0$ and $n = 1$, adopting the trigonal $R\bar{3}c$ structure illustrated in Fig. 1. The most well-known representative in this class is $Ca_3Co_2O_6$ where neighboring octahedral and trigonal prismatic sites are occupied by Co^{3+} in low ($S = 0$) and high ($S = 2$) spin states, respectively. The Co^{3+} in the trigonal prismatic coordination has a strong spin-orbit interaction and the coupling with the triangular lattice leads to the realization of a frustrated Ising state with only partial magnetic order [3,4]. In this instance, many exotic phenomena have been reported [5] and a complete theoretical understanding of the magnetic properties is still missing. The presence of a second magnetically active ion can break the inversion symmetry, as in Ca_3CoMnO_6, providing the perfect example of multiferroicity due to symmetric exchange [6].

Recently, the investigation of this family of compounds has been extended to ions belonging to the 5d family, mostly to understand the changes induced by the presence of an even larger spin-orbit coupling; one of the most interesting systems reported is Sr_3NiIrO_6 [7]. This compound, where Ni and Ir are magnetically active, presents many similarities with $Ca_3Co_2O_6$, with the spin-orbit anisotropy and the triangular arrangement in antiferromagnetically coupled chains, possibly at the origin of a loss of long-range ordering with decreasing temperature [8]. The most striking feature observed in Sr_3NiIrO_6 is the largest coercive field anisotropy (55 T) measured to date [9]. This peculiarity has been ascribed to the possibility of direct overlapping of the Ir 5d orbitals with the O 2p and Ni 3d orbitals.

Hence, in addition to the spin-orbit coupling, the spatial dimension of the magnetically active electronic cloud is crucial in establishing the magnetic behavior of the system. In 4d- and 5d-based oxides, the border between the localized and delocalized regime is closer than in the equivalent 3d-based system and such a feature has been indicated as a possible route to achieve high Néel temperatures, which may open entirely new scenarios in the realization of functional materials [10]. In this respect, a significant enhancement of the ordering temperatures has been observed between 3d systems such as Ca_3ZnMnO_6 ($T_N = 26$ K) [11] and 5d and 4d variants of $A_3A'BO_6$, with A = Ca,Sr; A' = Li,Na, and B = Os,Ru ($T_N = 70$–120 K) [12,13]. These contrasting ordering temperatures have been attributed to extended superexchange interactions that form between neighboring chains across multiple oxygen ions, removing frustration and helping to realize a

*dan.porter@diamond.ac.uk

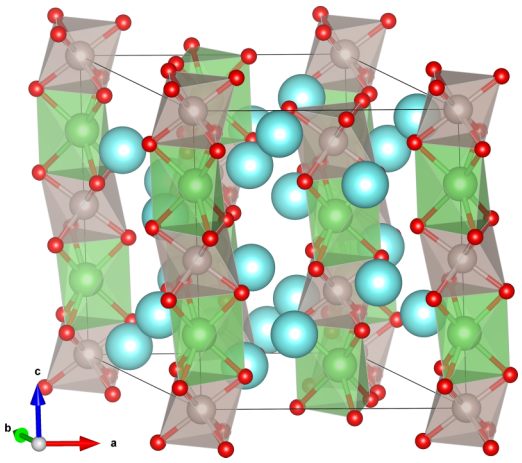

FIG. 1. Crystal structure of Sr_3ARuO_6 where gray spheres are Ru, green are Li or Na, blue are Sr, and red spheres are O. Bonds and polyhedra are displayed to clarify the chains of face sharing octahedra.

three-dimensional (3D) magnetic order [14,15]. It is therefore important to understand the microscopic mechanisms leading to the magnetic ordering in these compounds.

Here, we focus our attention on two members of this vast family of compounds, Sr_3LiRuO_6 and Sr_3NaRuO_6; both systems were previously reported together with their Ca-based counterpart [12]. Preliminary powder neutron diffraction measurements and laboratory measurements performed on Ca_3ARuO_6 (A = Li, Na) provided clear indications of long-range antiferromagnetic ordering in these materials, characterized by a propagation vector $\vec{k} = (0,0,0)$ and the appearance of several glide plane forbidden reflections with l = odd. Although neutron measurements were not performed on the Sr-based systems, Darriet [12] assumed an analogous magnetic ground state on the basis of the similar behavior of the magnetization in the Ca- and Sr-based systems. Due to the weakness of the observed reflections, Darriet could not fully establish the magnetic ground state, but concluded that the antiferromagnetic moment needed to have an in-plane component, and that a weak ferromagnetic moment existed in Ca_3LiRuO_6. More recently, Shi [13] and Calder [15] obtained similar results on the isostructural Ca_3LiOsO_6, which shows a similarly high Néel temperature. Although they managed to establish that the moment in this case is in the ab plane, they also could not solve completely the magnetic structure.

In this paper, after briefly describing the symmetric part of the magnetic exchange interaction at work in these systems, we provide a comprehensive study of the magnetic structure of Sr_3ARuO_6 with A = (Li,Na) based on neutron and x-ray magnetic scattering as well as on laboratory characterization. We confirm that the earlier findings apply also to the Sr-based systems, which are also adopting a ground state characterized by a propagation vector $\vec{k} = (0,0,0)$. We show that, in the limit that local anisotropy in this system is negligible, symmetric exchange alone is not able to choose the ground state. Using a symmetry-based analysis of the free-energy contributions, we identify the microscopic stabilization mechanism of the magnetic structure to be due to antisymmetric exchange, allowing for small ferromagnetic components both in-plane and along the c axis. This symmetry argument, together with the magnetization measurements, allows us to fully determine the magnetic moment direction, and it holds for all the systems mentioned in the previous paragraph.

II. CRYSTAL STRUCTURE AND SYMMETRY ANALYSIS

High-quality crystals of Sr_3LiRuO_6 and Sr_3NaRuO_6 were synthesized by solid-state reaction methods, as described in Ref. [16]. As grown, the Sr_3LiRuO_6 samples were typically small rods with dimensions $< 50 \times 50 \times 300$ μm^3 and < 0.5 mg in mass, the Sr_3NaRuO_6 samples were smaller at $< 50 \times 50 \times 100$ μm^3 and less than 0.2 mg. The crystallographic structure was checked using single-crystal x-ray diffraction on a molybdenum source supernova diffractometer (Oxford Diffraction). The refined structural parameters are given in Table I and are in good agreement with previous refinements of this structure [12,16,17]. As usual for this family of compounds, the crystals were all twinned by reticular merohedry, exhibiting reflections in both the obverse and reverse settings [18]. The crystallographic parameters of both systems are similar; they have essentially equivalent dimensions within the plane, although the Na system is expanded along the c axis by $\approx 4\%$. In both systems, a small distortion of the Ru-O octahedra is evident, with O-Ru-O bond angles deviating slightly from 90°. The Ru-O bond lengths are also very similar in both systems although there was no indication in either system of the oxygen bonds varying, implying little anisotropy in the Ru octahedra. The intrachain and interchain Ru-Ru distances, illustrated in Fig. 2, also only change in line with the small variation in lattice parameters.

We estimated the exchange couplings in Sr_3LiRuO_6 using the spin-dependent extended Hückel tight-binding (EHTB) method provided by the program CAESAR2 [19]. The results, illustrated in Fig. 3, reveal the relative strengths of the three nearest-neighbor interactions and are found to be directly correlated with the length of the Ru-Ru distances, as shown in Fig. 2. The calculation of J_1 gives the strongest interaction, while J_2 and J_3 have much weaker interactions at 0.46 J_1 and 0.22 J_1, respectively. All three interactions were antiferromagnetic. J_1 and J_2 interactions span a 3D network and act cooperatively, and hence alone account for long-range ordering in the system. The large value of J_2 compared to J_3 implies that the system is only weakly frustrated with J_3, allowing a large Néel temperature.

To determine the set of possible magnetic subgroups in this structure, representation analysis was performed using the ISODISTORT software [20]. At the Γ point, the space group $R\bar{3}c$ has three magnetic irreducible representations (IRs), named $m\Gamma_1^+$, $m\Gamma_2^+$, and $m\Gamma_3^+$, following the numbering scheme of Miller and Love [21]. Analysis of the magnetic modes associated with these IRs leads to the magnetic structures illustrated in Fig. 4. The totally symmetric $m\Gamma_1^+$ IR allows magnetic moments that keep the glide plane symmetry of the space group, where antiferromagnetic moments of Ru ions point along the c axis. In $m\Gamma_2^+$ the glide plane is odd with respect to time reversal and moments are ferromagnetic along the c axis, the structure is now described by the magnetic space group $R\bar{3}c'$. The $m\Gamma_3^+$ IR is activated by moments within the

TABLE I. Refined structure parameters of Sr_3LiRuO_6 and Sr_3NaRuO_6 using a supernova diffractometer with Mo source ($\lambda = 0.71$ Å). The structures were refined in the trigonal space group $R\bar{3}c$ (167) with positions Sr 18e : $(x, \frac{1}{3}, \frac{1}{12})$, Li/Na 6$a$: $(0,0,\frac{1}{4})$, Ru 6b : (0,0,0), and O 36f : (x,y,z). The obverse/reverse twin was defined with matrix ($\bar{1}00\ 0\bar{1}0\ 001$). Selected Ru bond lengths are given in Å, in particular, the Ru-Ru distances that associate to magnetic exchange paths J_1, J_2, and J_3.

		Sr_3LiRuO_6		Sr_3NaRuO_6	
		300 K	80 K	300 K	100 K
	a (Å)	9.633(1)	9.6202(7)	9.6261(4)	9.6086(5)
	c (Å)	11.0971(9)	11.0813(7)	11.5295(5)	11.5054(5)
Sr	x	0.02534(3)	0.02559(4)	0.02482(2)	0.02492(3)
	U_{iso}	0.00665(8)	0.00256(9)	0.00628(4)	0.00267(3)
A	U_{iso}	0.020(3)	0.011(3)	0.0090(3)	0.0041(2)
Ru	U_{iso}	0.00456(7)	0.00200(8)	0.00384(3)	0.00179(3)
O	x	0.1742(2)	0.1743(2)	0.1775(1)	0.1776(1)
	y	0.1528(2)	0.1524(2)	0.1547(1)	0.1549(1)
	z	0.1046(2)	0.1050(2)	0.0992(1)	0.0994(1)
	U_{iso}	0.0083(4)	0.0044(4)	0.0072(2)	0.0043(2)
	Twin vol.	0.994(5)	1.000(5)	0.75(2)	0.77(2)
	Ru-O	1.965(2)	1.964(2)	1.975(1)	1.974(1)
	Ru-Ru (J_1)	5.5486(9)	5.5406(7)	5.7648(5)	5.7527(5)
	Ru-Ru (J_2)	5.8612(6)	5.8532(5)	5.8805(3)	5.8696(3)
	Ru-Ru (J_3)	6.6795(6)	6.6703(5)	6.7570(3)	6.7441(3)
	O-Ru-O	88.66(7)	88.48(9)	89.82(6)	89.79(4)
	bond angles	91.34(7)	91.52(9)	90.18(6)	90.21(4)
	(degrees)	180.0(5)	180.0(5)	180.0(5)	180.0(5)
	R_w	2.66%	2.82%	3.24%	3.15%

ab plane. This IR is two dimensional with three symmetry distinct order-parameter directions. Two of these directions, resulting in the monoclinic $C2/c$ and $C2'/c'$ subgroups, allow the transition to be continuous. The third subgroup $P\bar{1}$ cannot be accessed directly from the paramagnetic state in the orbit space of the phenomenological Landau decomposition and, therefore, the associated transition is required to be necessarily first order. The continuous nature of the magnetic transitions in Sr_3ARuO_6 leaves us with the two monoclinic options for a further consideration. The $C2/c$ and $C2'/c'$ subgroups are separated by the collinear moment direction that activates them, being either along the glide plane of the original cell ($C2/c$), or perpendicular to it ($C2'/c'$). It should be noted, however, that in these IRs, the moment collinearity is not imposed by symmetry. These $C2/c$ and $C2'/c'$ subgroups can couple the $m\Gamma_1^+$ or $m\Gamma_2^+$ IRs, respectively, as secondary order parameters, potentially allowing small moments along the c axis.

III. MAGNETIC PROPERTIES

Characterization measurements were performed using individually mounted crystals. A Quantum Design PPMS was used for specific-heat measurements and magnetization measurements were performed using a Quantum Design MPMS 3, equipped with a SQUID magnetometer with a dc field. Zero-field cooled (ZFC) and field cooled (FC) measurements were performed in the presence of a 1000-Oe magnetic field from 30 to 100 K. The response to a magnetic field was measured by sweeping the external magnet between −50 and 50 kOe. In each case, the magnetization measurements were performed with the sample mounted with the c axis either parallel or perpendicular to the magnetic field. Given the small crystal dimensions, we estimate the possible error in orientation to be $< 5^\circ$.

The heat-capacity measurements, shown in Figs. 5(a) and 5(b), indicate second-order phase transitions at 90 K for Sr_3LiRuO_6 and 70 K for Sr_3NaRuO_6, in agreement with previously observed magnetic transitions. These phase transitions are of comparable magnitude to the exchange couplings calculated using EHTB. The same transitions are observed in the magnetization measurements, showing a small ferromagnetic response in either alignment [see Fig. 5(b)]. No difference was measured between ZFC and FC measurements, although it is possible that some small remnant field in the cryostat meant a true ZFC measurement was not possible. The recorded magnetic moment is one order of magnitude stronger when the sample is normal to the field direction.

The effective moment expected from a Ru^{5+}:$4d^3$ cation in an octahedral configuration is $3.87\mu_B$, assuming a completely quenched orbital magnetic component. Were all the Ru moments contributing, this would lead to a susceptibility of 21.6 emu/mol. This is more than two orders of magnitude greater than measured in the perpendicular geometry, implying most of the moments are antiferromagnetic and therefore not contributing to the ferromagnetic moment. A small remnant moment of $\approx 0.02\mu_B$ per Ru is measured in the absence of an applied field in the perpendicular case, indicating a small ferromagnetic moment remains within the *ab* plane [see Fig. 5(c)]. A similar remnant moment and small ferromagnetic response was reported by Darriet *et al.* although their measurements averaged over all crystal orientations.

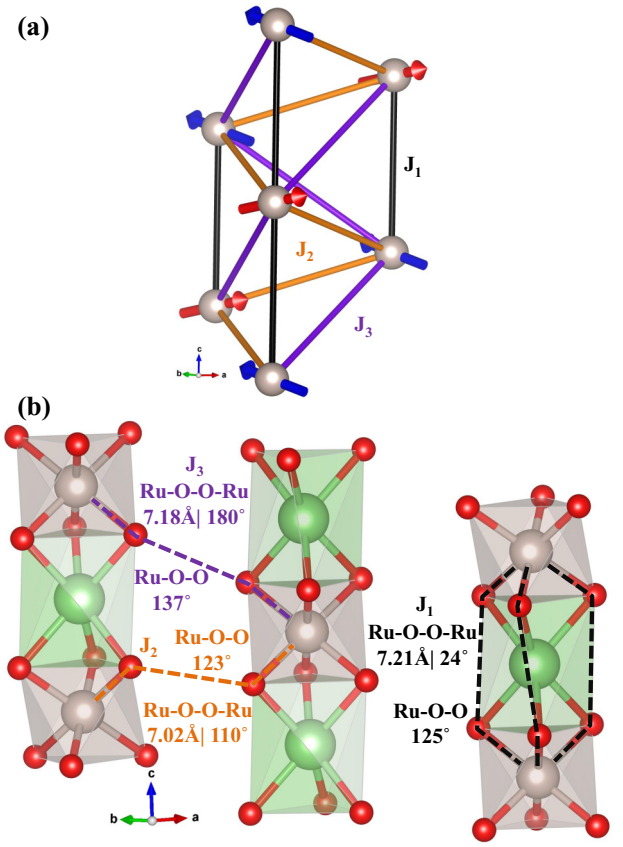

FIG. 2. Illustration of the possible exchange pathways in a cell of Sr_3ARuO_6. Gray spheres are Ru, green are Li or Na, and red spheres are O. The Sr ions have been removed for clarity. In (a), the three exchange paths are shown in the context of Ru-Ru bonds within the unit cell. In (b), dotted lines indicate the three Ru-O-O-Ru extended superexchange paths and are labeled in their respective color, along with their Ru-O-O-Ru path length and dihedral angle and Ru-O-O bond angle.

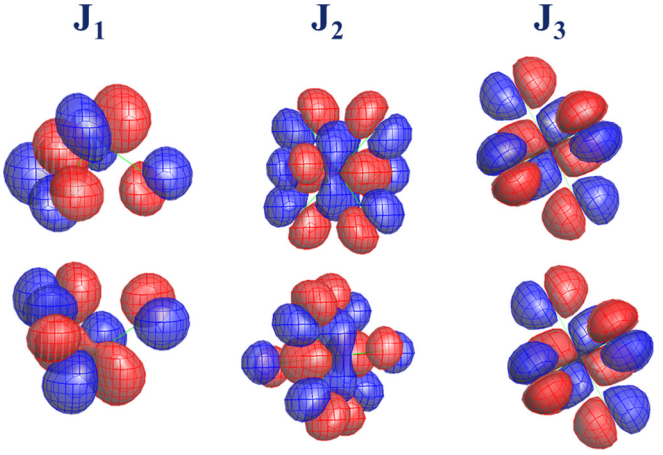

FIG. 3. Calculations from CAESAR2 indicating the highest occupied molecular orbital along each exchange path. Red and blue meshes illustrate orbitals around neighboring Ru ions. Orbitals generated for J_1 and J_2 are reflected between the ions as a result of antiferromagnetic exchange.

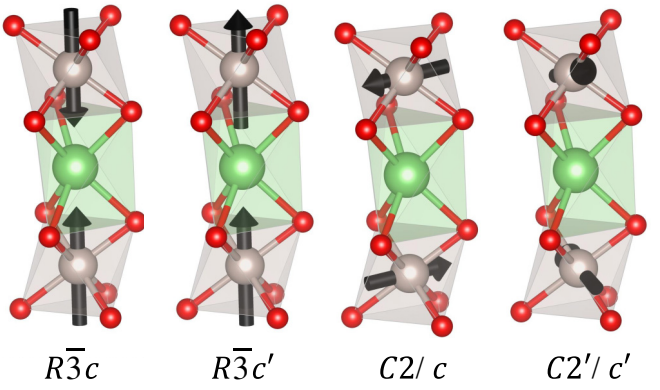

FIG. 4. Possible magnetic moments of the Ru ions. Each panel indicates the moment direction given by the possible magnetic space groups determined by representational analysis of the parent space group.

The Curie-Weiss parameters were determined from the high-temperature regions of the inverse susceptibility, providing estimates of the effective moment and Curie constant consistent with those previously reported [12].

In summary, the physical properties measurements indicate very similar magnetic behavior of both samples, with magnetic transitions occurring at elevated temperatures. A small ferromagnetic component is observed, predominantly within the *ab* plane, although this is only a fraction of the expected moment of system. Fits of the Curie parameters indicate the majority of the moment is antiferromagnetic and the estimated effective moment implies no sizable anisotropy from an orbital magnetic moment.

IV. NEUTRON MEASUREMENTS

Measurements were performed using the long-wavelength neutron diffractometer Wish [22] at the ISIS facility (UK). Due to the difficulty in producing a single phase powder by direct synthesis, a small, 5 mg powder sample was produced by grinding a small quantity of Sr_3LiRuO_6 single crystals. The sample was loaded into a cylindrical 3-mm-diameter vanadium can and measured at 100 and 1.5 K using an Oxford Instruments cryostat. The powder data were refined using the FULLPROF suite [23], including the use of the BASIREPS program [24] for definition of the magnetic modes. A nuclear model was refined based on the single-crystal x-ray refinement data, using the 100-K powder data. Additional peaks are apparent in the low-temperature data set (see Fig. 6) and these can be indexed on the same lattice, indicating a propagation vector $\vec{k} = (0,0,0)$, which is consistent with previous measurements of the Ca analog [12]. Refinements were made against the low-temperature data using the four possible magnetic models shown in Fig. 4. The ferromagnetic model is ruled out immediately by the presence of the large peak indexed as the {101} family of reflections and the in-plane antiferromagnetic models demonstrated better fits to the the data due to the presence of a weak peak at the (003) position. It was not possible to separate the two in-plane models due to the measured hexagonal cell showing no variation within the resolution limit of the present powder diffraction experiment. An illustration of the best fit obtained by an in-plane model

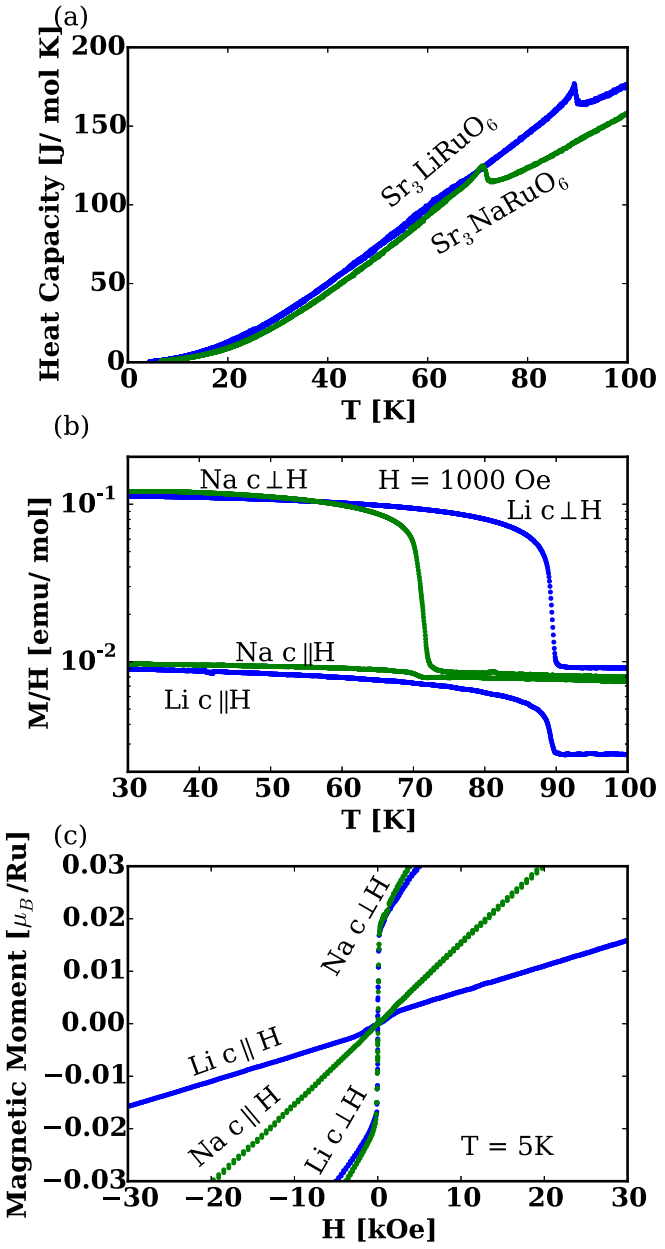

FIG. 5. Physical properties measurements of Sr_3LiRuO_6 and Sr_3NaRuO_6. In (a), the sample heat capacity indicates transitions at 90 and 70 K for the two samples, respectively. Susceptibility data in (b) indicate a weak ferromagnetic trend below the transitions with a stronger response when the field is perpendicular to the c axis; note that this plot is shown on a log scale for clarity of the smaller response with a parallel field. The field sweeps in (c) indicate a remnant magnetic moment when measured perpendicular to the c axis.

is given in Fig. 6. The ordered magnetic moment determined by the refinements was $2.03(3)\mu_B$, which is lower than the ordered magnetic moment expected for Ru^{5+}. Such a reduction of the static magnetic moment is often reported in systems with extended superexchange interactions, and is often attributed to fast fluctuations of the spin state.

Small crystals of Sr_3LiRuO_6 and Sr_3NaRuO_6 were also measured on Wish, though the small sample sizes ($50 \times 50 \times$ 500/300 μm^3, respectively) meant that long counting times were necessary. As exhibited in Fig. 7, several reflections were observed that disappeared above the magnetic transition temperature. Most important among these is the (003), a reflection forbidden by the structure's symmetry and also forbidden in the case of ferromagnetic scattering. Magnetic scattering can only appear at the (003) reflection if there is an antiferromagnetic component of the magnetic moment normal to this direction. Immediately this allows us to rule out two

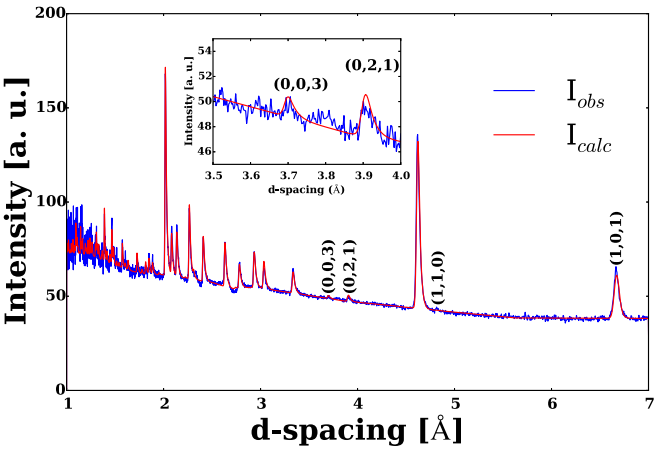

FIG. 6. Neutron powder pattern of Sr_3LiRuO_6 measured at 1.5 K with calculated diffraction pattern from the $C2'/c'$ magnetic model. Pure magnetic reflections are labeled. The inset magnifies the region showing the greatest variation between the models.

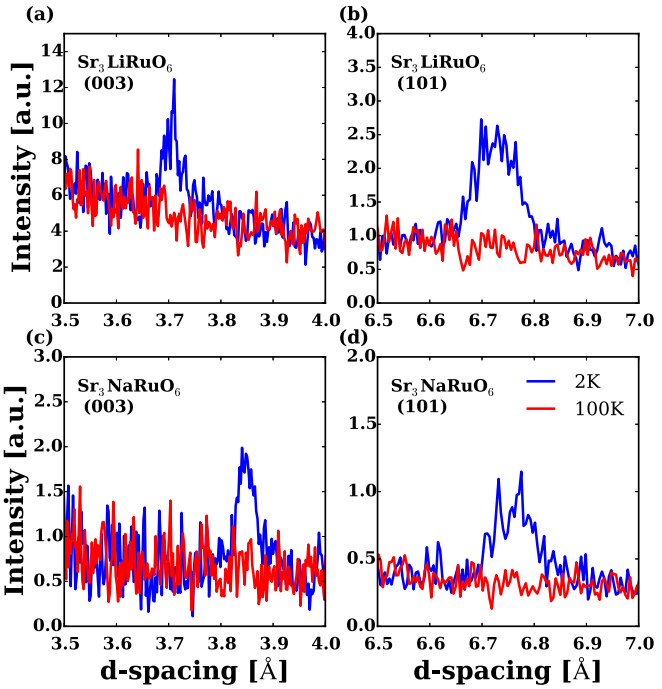

FIG. 7. Selected reflections from single-crystal neutron diffraction measurements of Sr_3LiRuO_6 and Sr_3NaRuO_6. In both systems, magnetic scattering occurs below the magnetic ordering temperature. The presence of scattering at the (0,0,3) reflection indicates that the moments have some component within the ab plane.

of the possible magnetic models described in Sec. II, as both $m\Gamma_1^+$ and $m\Gamma_2^+$ require the moment to be along the c axis and do not allow any in-plane component. Reflections at the (003) and (101) were both observed to disappear above the ordering temperature, as shown in Fig. 7. All of the ferromagnetic reflections have a nuclear component, however, we did not observe any variation in intensity below the transition in these reflections, including the weak nuclear (110) reflection, although the small size of sample could mean that a very weak ferromagnetic signal could have been missed. Within the instrument resolution, there was no evidence of split reflections arising from a small monoclinic distortion.

V. X-RAY MEASUREMENTS

Single crystals from the same batch as for the neutron measurements were studied on the materials and magnetism beamline, I16, at Diamond Light Source Ltd. [25]. Measurements were performed at the Ru L_3 absorption edge (2.838 keV) by reconfiguring the beamline for low energies, performing four bounces on the silicon monochromator, minimizing the air path, and extending the detector capability to low energies. At this energy, the focused spot size was $\approx 180 \times 50\ \mu\text{m}^2$. This is notably the first experiment on I16 in this energy range, effectively extending the beamline capability below the initial specifications. Samples were aligned in different geometries depending on the reflections measured. For reflections along the $\langle 00L\rangle$ direction, the samples were mounted as vertical rods, scattering from a very small $50 \times 50\ \mu\text{m}^2$, cleaved surface at the top of the rod. This arrangement gave access to reflections close to the $\langle 00L\rangle$ direction and had the advantage of providing a large azimuthal range at the (003) reflection. For other reflections, including those more sensitive to in-plane components, the samples were mounted flat, with the beam incident on the larger $\langle hh0\rangle$ surface of each sample. This arrangement gave a larger scattering surface which was less sensitive to movements of the cryostat and sample platform when changing temperature.

The polarization of the diffracted beam was linearly analyzed by rotating the scattering plane of a highly oriented (002) graphite plate. The cross-channel leakage of the analyzer crystal at this energy was $< 5\%$. The samples were measured in both vertical and horizontal beamline geometry, giving access to all four linear polarization channels, defined in Fig. 8. Using both geometries allowed us to take full advantage of the different sensitivities of the polarization cross sections present in resonant x-ray scattering. The Ru L_3 absorption edge is sensitive to the electric dipolar transition $2p_{3/2} \rightarrow 4d$, where the resonant elastic amplitudes are dependent on the polarization. The $E1$-$E1$ magnetic resonant x-ray scattering amplitudes can be expressed as [26]

$$f_{E1E1}^{mRXS} = \begin{pmatrix} \sigma-\sigma' & \sigma-\pi' \\ \pi-\sigma' & \pi-\pi' \end{pmatrix} = \begin{pmatrix} 0 & F_1\cos\theta + F_3\sin\theta \\ F_3\sin\theta - F_1\cos\theta & -F_2\sin 2\theta \end{pmatrix},$$

where θ is the Bragg angle and F_1, F_2, and F_3 are the Cartesian components of the magnetic scattering factor in the sample coordinate system, defined in Fig. 8.

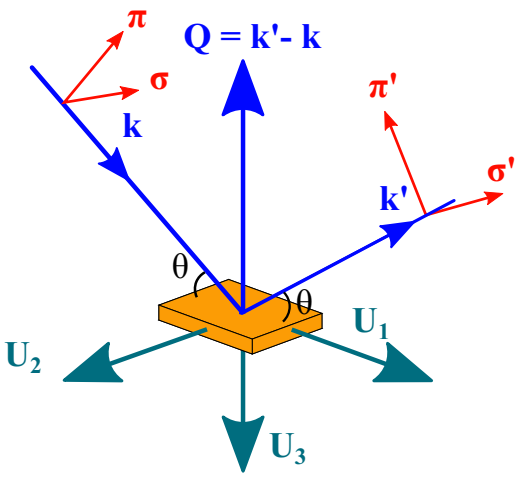

FIG. 8. Definitions of labels used in the description of resonant x-ray scattering measurements, where **U** is the sample coordinate system, **k** and **k**′ are the incident and outgoing wave vectors, π and σ are the polarization directions, θ is the Bragg angle, and **Q** is the wave-vector transfer.

Special consideration should be given to the effect the activation of the $m\Gamma_3^+$ IR, as the tensorial extinction rules of the system are dramatically changed when this representation is active. The magnetic symmetry allows now for three monoclinic domains, and even if the average global symmetry of the system is still in the parent group the electronic cloud distribution is no longer constrained by symmetry. The glide plane peaks, forbidden by the standard extinction rules in both monoclinic and pseudohexagonal crystal structures, are allowed in the high-symmetry trigonal phase only in the quadrupolar ($E2$) resonant channel, due to the threefold symmetry of the Ru sites, which forbids it in the dipole-dipole ($E1$-$E1$) channel. In the antiferromagnetic phase, if the threefold symmetry at the ruthenium site is broken, this $E1$-$E1$ channel becomes allowed. The amplitude of this signal will depend on the $4d$ DOS projected in directions determined by the incoming and outgoing polarizations so it will increase with the increase in the monoclinic distortion, however, in several cases it has been shown that such effects are already visible when the distortion is not yet visible by conventional diffraction [27]. The geometrical part of the nonmagnetic active spherical tensors in such situation are linear combinations of the $Y_{\pm 1}^1$ spherical harmonics.

Absorption from the cryostat's Be dome was found to remove the fluorescent background almost entirely, due to the higher absorption of the lower-energy fluorescent signal. As such, we performed an initial characterization of the fluorescence before the dome was fitted. Diffraction measurements were performed with the cryostat dome added and evacuated. We identified resonant peaks at charge forbidden reflections by scanning the incident beam energy across the resonant edge at a forbidden reflection defined using a reliable orientation matrix.

The resonant behavior of the magnetic reflection (021) at the Ru L_3 edge in Sr_3LiRuO_6 is shown in Fig. 9, along with the absorption coefficient determined from the fluorescence measurement. Once corrected for beam path and sample

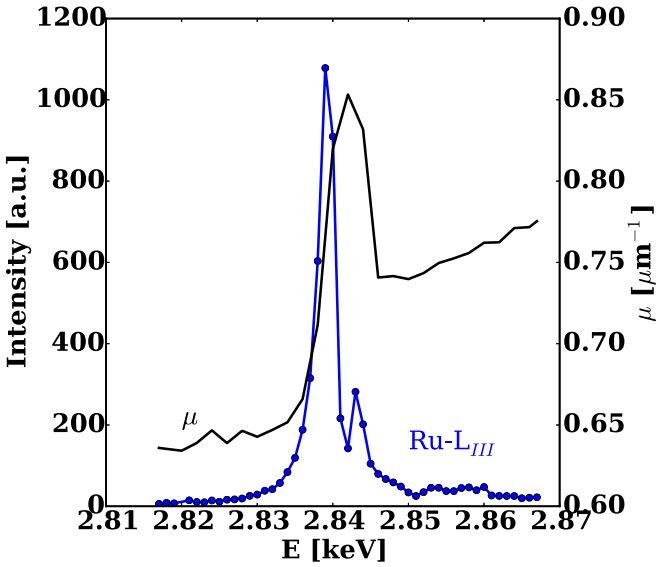

FIG. 9. Resonant x-ray diffraction measured at the Ru L_3 (2.83 keV) absorption edge at the magnetic (021) reflection in Sr_3LiRuO_6 at 8 K. The absorption coefficient μ was determined from fluorescence measured at 300 K.

absorption, the resonant behavior was the same for samples of both Sr_3LiRuO_6 and Sr_3NaRuO_6. Measurements were also made at the Ru L_2 edge (2.967 keV), and while the observed intensity was higher, the absorption is less at this higher energy and the corrected intensities were equivalent within the uncertainties of the corrections. The shape of the resonance is peculiar in this system due to the existence of the smaller secondary peak at higher energy (2.843 keV). Simulations of the dipolar $E1$-$E1$ resonance using the FDMNES software [28] show a qualitative agreement with this resonant shape. The ratio of the two peaks did not vary with azimuth, as such, there is no need to consider additional multipolar scattering processes.

A number of such resonances were found above weak reflections or extinctions and the polarization behavior of these reflections is illustrated in Fig. 10(b). The (101) and (003) reflections were present at extinction positions in both samples and their polarization appeared completely rotated, as the intensity was mainly found in the rotated σ-π' channel, with a small component in the σ-σ' channel due to leaked intensity from the analyzer. As with the neutron scattering results, these reflections are sensitive to antiferromagnetic moments, though here the reflections are sensitive to both moments within the plane and moments along the c axis. The (110) charge reflection is very weak due to near cancellation of the charge structure factors and is particularly sensitive to weak scattering phenomena. The L-even reflections are sensitive to ferromagnetic moments but the (110) is also a useful position to look for multipolar tensorial scattering brought on by a small monoclinic distortion arising from the onset of the $m\Gamma_3^+$ IR. This reflection was measured in horizontal geometry on the $\langle hh0\rangle$ surface, giving the advantage of reduced charge scattering and also access to the π-π' channel, which is sensitive to magnetic moments out of the scattering plane or, in this geometry, ferromagnetic moments along the c axis.

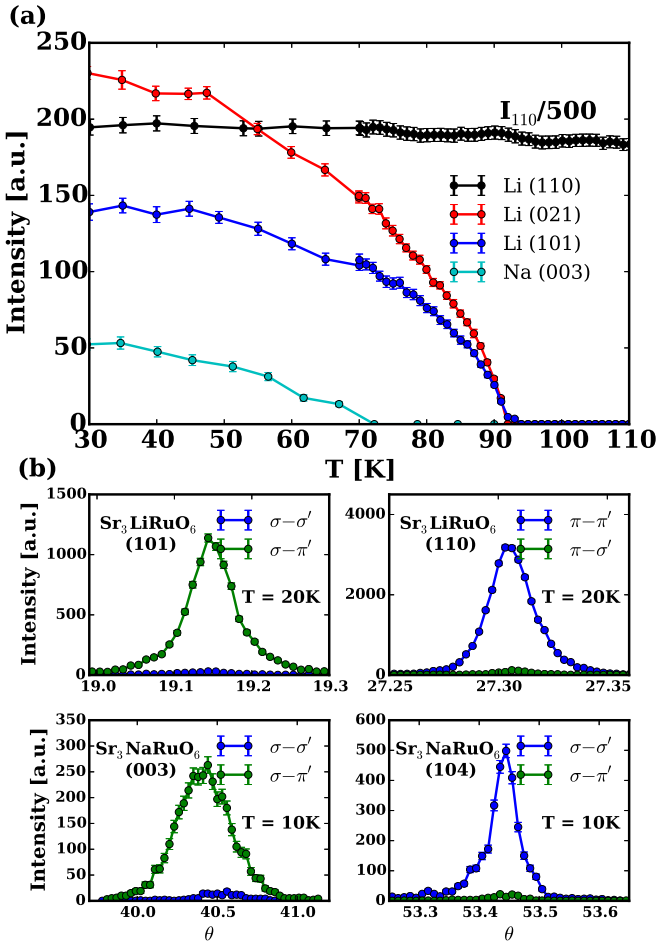

FIG. 10. Resonant x-ray diffraction measurements at the Ru L_3 edge showing temperature dependencies of magnetic reflections in (a) and the variation with polarization in (b). Left-hand panel reflections are magnetic in origin, and on the right hand, weakly allowed charge reflections are shown for comparison.

Polarization scans of this reflection found a strong signal in the π-π' channel and no discernible component in the π-σ' channel.

Each reflection was measured as a function of increasing temperature to verify the magnetic nature of the sample and establish the magnetic order parameter. The reflections were measured in the orientations described above in order to minimize variation of the surface position during sample heating. The reflections were measured at each temperature by performing a rocking scan with a Pilatus photon counting area detector, ensuring that the reflection did not become misaligned. The temperature dependencies, shown in Fig. 10(a), are in clear agreement with the physical properties measurements, with magnetic resonant reflections appearing at 90 K for Sr_3LiRuO_6 and 70 K for Sr_3NaRuO_6. The antiferromagnetic reflections (003), (101), and (021) have a typical thermal dependence of the order parameter and have no intensity above the ordering temperature. The weak charge reflection shows a subtle increase at the transition, consistent with the onset of a very small magnetic enhancement.

The spectral (003) reflection was measured as a function of azimuthal angle in both samples, realigning the sample and

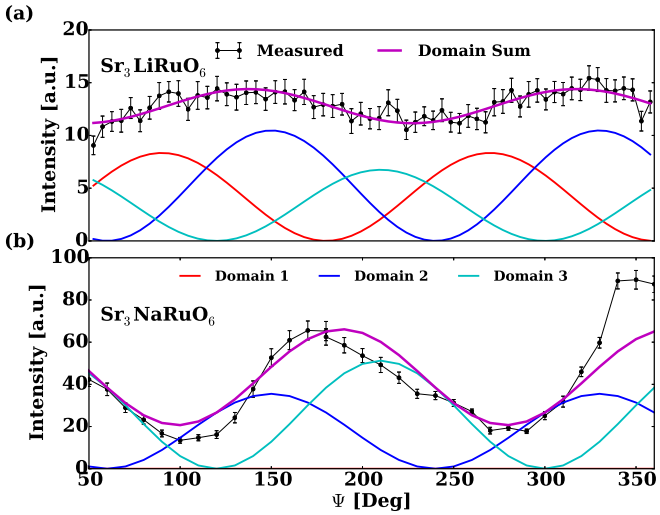

FIG. 11. Azimuthal dependencies of the resonant magnetic (003) reflection at 10 K of (a) Sr_3LiRuO_6 and (b) Sr_3NaRuO_6. The azimuthal angle ψ is the rotation around the wave-vector transfer, where $\psi = 0$ is defined along the projection of the $\langle h00 \rangle$ direction. Simulations of three trigonal domains from the antiferromagnetic in-plane model $C2'/c'$ are shown with the resulting summation that follows the observed data.

reflection at each step to counter the diffractometer sphere error and small sample size. At each azimuth, a rocking scan was performed with a Pilatus area detector to ensure small changes in the sample alignment were followed. The azimuthal dependencies shown in Fig. 11 appear to show different behaviors for the two samples, where the Sr_3LiRuO_6 reflection is essentially flat but the same reflection in Sr_3NaRuO_6 has a sinusoidal variation, although it should be noted that the minima of this curve do not reach zero intensity. A flat azimuthal dependence would be the signature of a moment laying along the c axis, however, neutron measurements exclude this possibility. Another way to interpret such a result is to consider multiple magnetic domains. On the (003) reflection we expect both the obverse and reverse domains to contribute according to their phase fraction, however, their azimuthal variation is identical. The in-plane moments of the $m\Gamma_3^+$ IR lower the symmetry to monoclinic. This monoclinic distortion can happen along any of the three trigonal directions, producing three possible magnetic domains separated by 120° rotations. Refining only the relative contributions of the three trigonal domains, it was possible to fit the azimuthal dependencies of both systems. It was not possible to distinguish between the two in-plane antiferromagnetic models as fitting different contributions of the two models would lead to the same fit of the data. The domain contributions for the two models, $C2/c$ and $C2'/c'$, are given in Table II. The possibility of multiple domains contributing to azimuthal dependencies is often neglected in analysis of resonant x-ray experiments, as most of the time a single magnetic domain is much larger than the beam size. Our results clearly indicate that this is certainly not the case in these compounds and careful consideration of such possibilities can result in a completely different conclusion with respect to the magnetic structure inferred by the experimental data set for a monodomain sample. Interestingly, while in the

TABLE II. Domain contributions to azimuthal dependencies of Sr_3LiRuO_6 and Sr_3NaRuO_6.

	Domain	$C2/c$	$C2'/c'$
Sr_3LiRuO_6	1	34%	33%
	2	26%	41%
	3	40%	26%
Sr_3NaRuO_6	1	74%	0%
	2	21%	41%
	3	5%	59%

Sr_3LiRuO_6 case the data could be fitted also using a single magnetic domain, although reaching a wrong conclusion about the moment direction, the results obtained from Sr_3NaRuO_6 are particularly important as it is not possible to obtain an acceptable fit within a single magnetic domain, even neglecting all the symmetry consideration and allowing large moment canting. The presence of almost equipopulated magnetic domain size in the case of the Li points to micrometric or submicrometric domains, whereas the different domain fractions in the Na case seem to point to larger domain size even if still smaller than the beam size. In the presence of a subtle monoclinic distortion, similar domain sizes were recently reported in Ref. [29].

VI. ANALYSIS

Our estimate of the symmetric exchange integral values are consistent with the experimental finding of a magnetic ground state with antiferromagnetic J_1 and J_2 exchange integrals, described in Fig. 2(a). However, the Heisenberg symmetric exchange interactions alone are degenerate in respect of a global rotation of the magnetic structure, hence, the corresponding part of the exchange energy does not depend on the spatial direction of the interacting spins.

It is hence crucial to rationalize the origin of the magnetic structure to understand the role played by the higher-order anisotropic terms in the magnetic Hamiltonian such as antisymmetric exchange and single-ion anisotropy in removing the global spin rotation degeneracy, making some crystallographic directions preferable.

As these terms are hardly accessible experimentally a powerful method is to approach the problem from the point of view of group theory and establish which terms are symmetry allowed and needed in the free-energy expansion to completely lift the ground-state degeneracy. Once the invariant terms have been formally written, by inspection it is possible to relate each term to a specific physical interaction.

A detailed description of this approach is given in the Appendix where we show that the in-plane spin configuration with the $C2'/c'$ magnetic symmetry is energetically favorable and can be physically understood considering the antisymmetric Dzyaloshinskii-Moriya (DM) exchange as the dominant anisotropic interaction in the system.

As shown in the Appendix, the antisymmetric interactions can be divided into two types. The first one is imposed by structural distortions unrelated to magneto-elastic coupling. This part is described by a third-power free-energy invariant

which couples in-plane antiferromagnetic and ferromagnetic components and it lifts the degeneracy between $R\bar{3}c$ and the in-plane configurations. This part is degenerate in respect of the spin direction within the ab plane and therefore cannot select between the $C2'/c'$ and $C2/c$ magnetic space groups. The second type of the antisymmetric exchange couples in-plane antiferromagnetic and out-of-plane ferromagnetic components and is imposed by the distortions induced through the magnetoelastic coupling. It is described by the fifth-power free-energy term and is activated only by the in-plane antiferromagnetic configuration with the $C2'/c'$ symmetry. Experimentally, there is a weak signature of this out-of-plane ferromagnetic component visible in the magnetometry measurements in Fig. 4(c).

VII. CONCLUSION

Our results prove that antisymmetric exchange is crucial in establishing the ground state of this family of compounds. In the absence of local anisotropy, the degeneracy of the ground state between the in-plane directions of the magnetic moment is lifted by a fifth-order term in the free-energy expansion coupling in-plane antiferromagnetism with a ferromagnetic component along the c axis. In the compounds studied here, this result is confirmed by the behavior of the magnetization both along the c axis and within the ab plane. The same expansion of the free energy will apply to similar systems, the only caveat for such results being the absence of a competing single-ion anisotropy. For this reason, in similar systems magnetization measurements alone will provide an important insight on the choice of the ground state. The absence of monoclinic distortion and the small value of the ferromagnetic moment point to the weakness of the DM term, in such respect it would be interesting to analyze the response of these systems to an external magnetic field, that could provide a handle to rotate the magnetization.

ACKNOWLEDGMENTS

We acknowledge Diamond Light Source for time on Beamline I16 under Proposal No. 9409. We acknowledge ISIS for time on the instrument Wish under Proposal No. 1520273. Work at ISIS was supported by project TUMOCS. This project has received funding from the European Union's Horizon 2020 research and innovation programme under the Marie Skłodowska-Curie Grant Agreement No. 645660. H.z.L. and A.C. acknowledge support from the NSF via Award No. DMR-1301757. C.M. thanks Diamond Light Source for their hospitality during this work. Images of atomic structures were created using the computer program VESTA, by K. Momma and F. Izumi [30].

TABLE III. Atomic components of basis function of irreducible representation of $R\bar{3}m1'$ localized on the Ru $3a(0,0,0)$ site.

mT_3^+		$m\Gamma_3^+$		$m\Gamma_2^+$
η_1	η_2	ξ_1	ξ_2	μ
$\begin{pmatrix}1\\1\\0\end{pmatrix}$	$\begin{pmatrix}\frac{1}{\sqrt{3}}\\-\frac{1}{\sqrt{3}}\\0\end{pmatrix}$	$\begin{pmatrix}1\\0\\0\end{pmatrix}$	$\begin{pmatrix}\frac{1}{\sqrt{3}}\\\frac{2}{\sqrt{3}}\\0\end{pmatrix}$	$\begin{pmatrix}1\\0\\0\end{pmatrix}$

APPENDIX: SYMMETRY ANALYSIS

We follow the procedure developed in Refs. [31–33] to analyze DM interactions in some Fe^{3+}-based distorted perovskites. The procedure exploits the fact that antisymmetric exchange is a coupling phenomenon imposed by structural distortions. It couples orthogonal spin modes and is activated when spins in the primary mode take specific directions in the crystal such that the midpoint between the interacting spins no longer possess a center of inversion [34].

This analysis is based on coupling trilinear free-energy terms invariant in respect of a supergroup symmetry, where the orthogonal spin modes transform by different irreducible representations. These energy terms combine the spin modes with the appropriate structural distortions, or atomic displacement modes, which are responsible for the coupling. This approach allows one to identify the relevant structural distortions and to make a quantitative comparison between different coupling schemes imposed by different displacement modes.

The paramagnetic crystal structure of Sr_3LiRuO_6 has the $R\bar{3}c1'$ symmetry and the experimentally found in-plane antiferromagnetic configuration is bilinearly coupled to the in-plane ferromagnetic component. The supergroup which decouples these spin configurations is $R\bar{3}m1'$ with only half of the translation along the c axis. This is the symmetry of the Ru

TABLE IV. Matrix of irreducible representation from generators of the $R\bar{3}m1'$ space group associated with Γ $[\vec{k}=(0,0,0)]$ and T $[\vec{k}=(0,0,3/2)]$ points of symmetry. t is the time-reversal operator.

Irrep	$\{-3+\|0,0,0\}$	$\{2_x\|0,0,0\}$	$\{1\|2/3,1/3,1/3\}$	$\{1\|1/3,2/3,2/3\}$	$\{1\|0,0,1\}$	t
$m\Gamma_2^+(\mu)$	1	-1	1	1	1	-1
$m\Gamma_3^+(\xi_1,\xi_2)$	$\begin{pmatrix}-\frac{1}{2}&-\frac{\sqrt{3}}{2}\\\frac{\sqrt{3}}{2}&-\frac{1}{2}\end{pmatrix}$	$\begin{pmatrix}1&0\\0&-1\end{pmatrix}$	$\begin{pmatrix}1&0\\0&1\end{pmatrix}$	$\begin{pmatrix}1&0\\0&1\end{pmatrix}$	$\begin{pmatrix}1&0\\0&1\end{pmatrix}$	$\begin{pmatrix}-1&0\\0&-1\end{pmatrix}$
$mT_3^+(\eta_1,\eta_2)$	$\begin{pmatrix}-\frac{1}{2}&\frac{\sqrt{3}}{2}\\-\frac{\sqrt{3}}{2}&-\frac{1}{2}\end{pmatrix}$	$\begin{pmatrix}-\frac{1}{2}&\frac{\sqrt{3}}{2}\\\frac{\sqrt{3}}{2}&\frac{1}{2}\end{pmatrix}$	$\begin{pmatrix}-1&0\\0&-1\end{pmatrix}$	$\begin{pmatrix}1&0\\0&1\end{pmatrix}$	$\begin{pmatrix}-1&0\\0&-1\end{pmatrix}$	$\begin{pmatrix}-1&0\\0&-1\end{pmatrix}$
$\Gamma_3^+(\sigma_1,\sigma_2)$	$\begin{pmatrix}-\frac{1}{2}&-\frac{\sqrt{3}}{2}\\\frac{\sqrt{3}}{2}&-\frac{1}{2}\end{pmatrix}$	$\begin{pmatrix}1&0\\0&-1\end{pmatrix}$	$\begin{pmatrix}1&0\\0&-1\end{pmatrix}$	$\begin{pmatrix}1&0\\0&1\end{pmatrix}$	$\begin{pmatrix}1&0\\0&1\end{pmatrix}$	$\begin{pmatrix}1&0\\0&1\end{pmatrix}$
$T_2^+(\delta)$	1	-1	1	1	-1	1

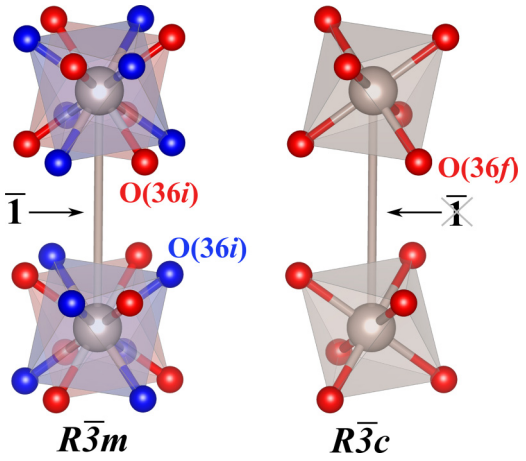

FIG. 12. Ru-O-O-Ru super-superexchange bond in the $R\bar{3}m$ (a) and $R\bar{3}c$ (b) structures. Oxygen in the $R\bar{3}m$ structure occupies $36i$[0.1742(2),0.1528(2),0.2092(4)] Wyckoff position with the occupancy 0.5. In the $R\bar{3}c$ structure the oxygen position splits into two independent sites shown by different colors, $36f$[0.1742(2),0.1528(2),0.1046(2)] (occupied) and $36f$[0.1742(2),0.02140(2),0.1045(2)], vacant.

sublattice without environment and electronic anisotropy of the Ru atoms. Ru occupies the $3a$ Wyckoff position in $R\bar{3}m1'$ and the in-plane antiferromagnetic and ferromagnetic spin modes are transformed by the two-dimensional $mT_3^+(\eta_1,\eta_2)$ and $m\Gamma_3^+(\xi_1,\xi_2)$ irreducible representations of $R\bar{3}m1'$, respectively (Tables III and IV). Γ and T relate to the $\vec{k}=(0,0,0)$ and $\vec{k}=(0,0,3/2)$ points of symmetry, respectively. To combine them into a free-energy invariant, structural distortions with the $T_2^+(\delta)$ symmetry need to be added:

$$\delta\xi_1\eta_1 - \frac{1}{\sqrt{3}}\delta\xi_1\eta_2 - \frac{1}{\sqrt{3}}\delta\xi_2\eta_1 - \delta\xi_2\eta_2. \qquad \text{(A1)}$$

These structural distortions reduce the symmetry from $R\bar{3}m1'$ down to $R\bar{3}c1'$ and locally they play the role of Dzyaloshinskii vector $\vec{D}_{ij}$ for pairs of interacting spins $\vec{S}_i$ and $\vec{S}_j$. In the $R\bar{3}m1'$ supergroup, oxygen is disordered over the $36i$ Wyckoff position and the midpoint between the Ru^{5+} ions poses a center of inversion. The one-dimensional order parameter $T_2^+(\delta)$ has several physical realizations (distortion types). The order-disorder scalar-type splits the $36i$ oxygen position into two $36f$ positions, one of which is fully occupied and another is empty in the $R\bar{3}c1'$ structure (Fig. 12). This removes the inversion center activating the antisymmetric exchange. Another realization of the $T_2^+(\delta)$ order parameter is a rotation of the RuO_6 polyhedra about the c axis. This pseudovector type of distortions also modifies the Ru-O-O-Ru super-superexchange paths and activates antisymmetric exchange.

The two antiferromagnetic in-plane configurations with the $C2/c$ and $C2'/c'$ magnetic space groups, discussed in Sec. II, occur when the order parameter in the mT_3^+ representation space takes the $mT_3^+(\eta_1,0)$ and $mT_3^+(0,\eta_2)$ directions, respectively. They couple the corresponding orthogonal ferromagnetic components with the $(\frac{\sqrt{3}}{2}\xi_1, -\frac{1}{2}\xi_1)$ and $(-\frac{1}{2}\xi_1, -\frac{\sqrt{3}}{2}\xi_1)$ order parameters in the $m\Gamma_3^+$ representation space. In both cases, the free-energy term (A1) reduces down to the product $\frac{2}{\sqrt{3}}\delta\xi\eta$, indicating that both configurations $C2'/c'$ and $C2/c$ are degenerate in respect of this part of the antisymmetric exchange.

The out of-plane ferromagnetic component is transformed by the $m\Gamma_2^+(\mu)$ irreducible representation of $R\bar{3}m1'$ and cannot be coupled to the in-plane antiferromagnetic configuration through the trilinear invariant similar to that specified above. Thus, the system adopts the in-plane spin configuration to activate the coupling term (A1) and gains energy from the antisymmetric exchange imposed by the structural distortions reducing the symmetry from $R\bar{3}m1'$ down to $R\bar{3}c1'$.

To further compare the $C2'/c'$ and $C2/c$ magnetic space groups, let us consider higher-order free-energy terms. In this respect, the fifth-power invariant

$$\delta\mu\eta_1^3 - 3\delta\mu\eta_1\eta_2^2 \qquad \text{(A2)}$$

is particularly important since it breaks the degeneracy between the two in-plane spin configurations. It couples the out-of-plane ferromagnetic component μ in the case of the $(\eta_1,0)$ order-parameter direction ($C2'/c'$ symmetry) and it vanishes for the $(0,\eta_2)$ direction ($C2/c$ symmetry). To understand which microscopic interactions are behind this energy term, let us rewrite the nonvanishing part $\delta\mu\eta_1^3 \equiv \delta\mu\eta^3$ as $\delta\mu\eta\eta^2$. The latter includes the product of μ (ferromagnetic) and η (antiferromagnetic) order parameters as in the case of antisymmetric DM exchange interactions. In addition, it contains η^2 which is known to represent magnetoelastic coupling. The general magnetoelastic coupling term is written as

$$\frac{1}{2\sqrt{3}}\sigma_1\eta_1^2 - \sigma_1\eta_1\eta_2 - \frac{1}{2\sqrt{3}}\sigma_1\eta_2^2 + \frac{1}{2}\sigma_2\eta_2^2 + \frac{1}{\sqrt{3}}\sigma_2\eta_1\eta_2 - \frac{1}{2}\sigma_2\eta_2^2, \qquad \text{(A3)}$$

where σ_1 and σ_2 are components of the order parameter transformed by the time-even Γ_3^+ representation. This term reduces down to $\frac{1}{2\sqrt{3}}\sigma_1\eta^2 + \frac{1}{2}\sigma_2\eta^2$ for the $(\eta,0)$ order-parameter direction and couples the $(\frac{1}{2\sqrt{3}}\sigma, \frac{1}{2}\sigma)$ direction in Γ_3^+. The $(\frac{1}{2\sqrt{3}}\sigma, \frac{1}{2}\sigma)$ order parameter represents the symmetry-breaking monoclinic strains and oxygen displacement mode which both reduce the symmetry from $R\bar{3}m1'$ down to $C2/m1'$. The transformational properties of these quantities are identical to η_2 and, therefore, the fifth-power term $\delta\mu\eta\eta^2$ can be transformed to the fourth power $\delta\sigma\mu\eta$, which describes the magnetoelastically induced antisymmetric exchange.

[1] Q. Zhao, J. Darriet, M.-H. Whangbo, L. Ye, C. Stackhouse, and H.-C. zur Loye, J. Am. Chem. Soc. **133**, 20981 (2011).

[2] H.-C. zur Loye, Q. Zhao, D. E. Bugaris, and W. M. Chance, CrystEngComm. **14**, 23 (2012).

[3] S. Agrestini, C. Mazzoli, A. Bombardi, and M. R. Lees, Phys. Rev. B **77**, 140403 (2008).
[4] S. Agrestini, L. C. Chapon, A. Daoud-Aladine, J. Schefer, A. Gukasov, C. Mazzoli, M. R. Lees, and O. A. Petrenko, Phys. Rev. Lett. **101**, 097207 (2008).
[5] S. Agrestini, C. L. Fleck, L. C. Chapon, C. Mazzoli, A. Bombardi, M. R. Lees, and O. A. Petrenko, Phys. Rev. Lett. **106**, 197204 (2011).
[6] Y. J. Choi, H. T. Yi, S. Lee, Q. Huang, V. Kiryukhin, and S. W. Cheong, Phys. Rev. Lett. **100**, 047601 (2008).
[7] T. N. Nguyen and H.-C. zur Loye, J. Solid State Chem. **117**, 300 (1995).
[8] E. Lefrançois, L. C. Chapon, V. Simonet, P. Lejay, D. Khalyavin, S. Rayaprol, E. V. Sampathkumaran, R. Ballou, and D. T. Adroja, Phys. Rev. B **90**, 014408 (2014).
[9] J. Singleton, J. W. Kim, C. V. Topping, A. Hansen, E.-D. Mun, S. Ghannadzadeh, P. Goddard, X. Luo, Y. S. Oh, S.-W. Cheong, and V. S. Zapf, arXiv:1408.0758.
[10] S. Middey, S. Debnath, P. Mahadevan, and D. D. Sarma, Phys. Rev. B **89**, 134416 (2014).
[11] S. Kawasaki, M. Takano, and T. Inami, J. Solid State Chem. **145**, 302 (1999).
[12] J. Darriet, F. Grasset, P. D. Battle, C. Brivazac, A. Schweitzer, and P. Cedex, Mater. Res. Bull. **32**, 139 (1997).
[13] Y. Shi, Y. Guo, S. Yu, M. Arai, A. Sato, A. a. Belik, K. Yamaura, and E. Takayama-Muromachi, J. Am. Chem. Soc. **132**, 8474 (2010).
[14] E. Kan, F. Wu, C. Lee, J. Kang, and M. H. Whangbo, Inorg. Chem. **50**, 4182 (2011).
[15] S. Calder, M. D. Lumsden, V. O. Garlea, J. W. Kim, Y. G. Shi, H. L. Feng, K. Yamaura, and A. D. Christianson, Phys. Rev. B **86**, 054403 (2012).
[16] M. J. Davis, M. D. Smith, K. E. Stitzer, and H.-C. zur Loye, J. Alloys Compd. **351**, 95 (2003).
[17] S. Frenzen and Hk. Müller-Buschbaum, Z. Naturforsch. **50b**, 581 (1995).
[18] R. Herbst-Irmer and G. M. Sheldrick, Acta Crystallogr., Sect. B **58**, 477 (2002).
[19] J. Ren and M.-H. Whangbo, CAESAR 2.0 Primecolor Software, Inc., Madison, WI, 1998.
[20] B. J. Campbell, H. T. Stokes, D. E. Tanner, and D. M. Hatch, J. Appl. Crystallogr. **39**, 607 (2006).
[21] A. P. Cracknell, B. L. Davies, S. C. Miller, and W. F. Love, *Kronecker Product Tables. Vol. 1: General Introduction and Tables of Irreducible Representations of Space Groups* (IFI/Plenum, New York, 1979).
[22] L. C. Chapon, P. Manuel, P. G. Radaelli, C. Benson, L. Perrott, S. Ansell, N. J. Rhodes, D. Raspino, D. Duxbury, E. Spill, and J. Norris, Neutron News **22**, 22 (2011).
[23] J. Rodriguez-Carvajal, Phys. B (Amsterdam) **192**, 55 (1993).
[24] J. Rodriguez-Carvajal, http://www.ill.eu/sites/fullprof/
[25] S. P. Collins, A. Bombardi, A. R. Marshall, J. H. Williams, G. Barlow, A. G. Day, M. R. Pearson, R. J. Woolliscroft, R. D. Walton, G. Beutier, and G. Nisbet, AIP Conf. Proc. **1234**, 303 (2010).
[26] J. P. Hill and D. F. McMorrow, Acta Crystallogr., Sect. A **52**, 236 (1996).
[27] A. Bombardi, F. de Bergevin, S. D. Matteo, L. Paolasini, P. Metcalf, and J. Honig, Phys. B (Amsterdam) **345**, 40 (2004).
[28] O. Bunau and Y. Joly, J. Phys.: Condens. Matter **21**, 345501 (2009).
[29] N. Waterfield-Price, R. D. Johnson, W. Saenrang, F. Maccherozzi, S. S. Dhesi, A. Bombardi, F. P. Chmiel, C. B. Eom, and P. G. Radaelli, Phys. Rev. Lett. (to be published).
[30] K. Momma and F. Izumi, J. Appl. Crystallogr. **44**, 1272 (2011).
[31] D. D. Khalyavin, A. N. Salak, N. M. Olekhnovich, A. V. Pushkarev, Y. V. Radyush, P. Manuel, I. P. Raevski, M. L. Zheludkevich, and M. G. S. Ferreira, Phys. Rev. B **89**, 174414 (2014).
[32] D. D. Khalyavin, A. N. Salak, P. Manuel, N. M. Olekhnovich, A. V. Pushkarev, Y. V. Radysh, A. V. Fedorchenko, E. L. Fertman, V. A. Desnenko, and M. G. Ferreira, Z. Kristallogr. **230**, 767 (2015).
[33] D. D. Khalyavin, A. N. Salak, A. B. Lopes, N. M. Olekhnovich, A. V. Pushkarev, Y. V. Radyush, E. L. Fertman, V. A. Desnenko, A. V. Fedorchenko, P. Manuel, A. Feher, J. M. Vieira, and M. G. S. Ferreira, Phys. Rev. B **92**, 224428 (2015).
[34] T. Moriya, Phys. Rev. **120**, 91 (1960).